Polarized Self-Absorption

A potential new method for probing excited states of nuclei

By
Nicholas Walton
Senior Honors Thesis
Department of Physics and Astronomy
University of North Carolina at Chapel Hill

April 5, 2023

Approved:

Robert Janssens: Thesis Advisor

Louise Dolan: Reader

Akaa Ayangeakaa: Reader

ABSTRACT

Photon strength functions are some of the most important and useful properties of nuclei. Their uses range from modeling the synthesis of light and heavy elements in supernovae to the production of medical isotopes to be used in imaging and therapy. However, complete knowledge of all possible decay modes of a nucleus is required before these functions can be calculated. Current methods of probing nuclei, such as nuclear resonance fluorescence (NRF), often fail to find low-energy decays due to exponentially increasing background radiation at low energies. As a result, current knowledge of all possible decays of a nucleus results in a lower limit rather than a definitive value. I seek to probe the reliability of Polarized Self Absorption, a new method proposed for probing nuclei that takes advantage of the quasi-monochromatic and linearly polarized photon beam produced at the High Intensity γ-ray Source, by examining the 10.71-MeV excited state in ^{24}Mg. Specifically, I work towards finding the full and partial widths of this state in ^{24}Mg. As a first result, this work found new decay paths out of the 10.71-MeV state and determined its spin and parity to be 1^+. The difference between the experimental asymmetry, $\bar{A}_{Ex} = 0.644(5)$, and the mass-weighed asymmetry, $\bar{A}_{MW} = 0.457(5)$, indicates that self absorption is taking place, as required for this method to work. However, the final determination of the resonance width will have to await resolution of an issue discussed further in the text.

I. INTRODUCTION

Modern nuclear-structure physics research is dominated by understanding the many characteristics of excited states of nuclei, as such states provide physicists a window into explaining the forces that bind nucleons together to form a nucleus. Today, this is done with a number of approaches among which figures nuclear resonance fluorescence (NRF) experiments. NRF experiments involve resonantly exciting a nucleus to an excited state with a photon. After a short period of time, the nucleus will decay to a lower state by emitting one or several additional gamma rays. By measuring these emitted gamma rays, physicists can learn many properties of a nucleus' excited state such as its spin, parity, and resonance width. Further understanding of these properties allows theorists to test current models of the nuclear force.

An accurate model of all decays of an isotope involves the photon strength function (PSF), which gives the average γ-ray transition probability at a given excitation energy, E [1]. At low energies, the nuclear level density of most isotopes is low, allowing for physicists to probe one excited state at time. However, as the excitation energy increases, the number of states rises rapidly to the extent that even the best detectors are unable to observe individual levels [1]. Hence, a different approach in terms of γ-ray transition probability as a function of excitation energy is required. In astrophysics, the PSF is used for modeling the synthesis of light and heavy elements in supernovae or neutron-star mergers [2, 3]. Other uses include a greater understanding of an isotope's nuclear structure, medical isotope production, the transmutation of nuclear waste, and fission and fusion reactors [3, 4].

The primary setback of the NRF method is a need for the total resonance width, Γ_i, for a given state i. To derive the PSF, two quantities are required. The first one is the energy-integrated elastic cross section. For a nucleus initially in its 0^+ ground state resonantly excited to one of its excited states i, then decaying back to its ground state, the energy-integrated elastic cross section, $I_{0 \to i \to 0}$, is proportional to

$$I_{0 \to i \to 0} \propto \Gamma_{i \to 0} \frac{\Gamma_{i \to 0}}{\Gamma_i} \tag{1}$$

where $\Gamma_{i\to 0}$ is the partial width for the ground-state decay, and Γ_i is the total resonance width

$$\Gamma_i = \sum_{j\in J} \Gamma_{i\to j} \tag{2}$$

where $\Gamma_{i\to j}$ is the partial width for the decay from excited state i to final state j, and J contains all possible decays from state i [5, 6]. Second is the energy-integrated photoabsorption cross section. For an excitation from the ground state 0 to a generic excited state, i, the energy-integrated photoabsorption cross section, $I_{0\to i}$ is:

$$I_{0\to i} \propto \Gamma_{i\to 0} \tag{3}$$

where $\Gamma_{i\to 0}$ is the partial width for the decay to the ground state [3, 6]. With Eqs. 1, 2, and 3, it can be seen that, to properly know the PSF, knowledge of all possible decays from all excited states is required.

Absolute knowledge of the cross sections involved is primarily done with a bremsstrahlung beam, which generates a beam of photons up to a desired energy, allowing for cross sections of multiple decay cascades to be measured simultaneously [3]. While using a bremsstrahlung beam can save time, the wider energy range also contains photons with nonresonant energies. As a result, NRF experiments have exponentially increasing background radiation at lower energies, causing low-energy decays to often be overlooked in proper cross section evaluations. This means that any $I_{0\to i\to 0}$ reported from such NRF experiments are, in fact, lower limits rather than definitive values [6].

Another issue inherent to NRF is the atomic absorption effect. As the photon beam passes through a target, photons of resonant energies are going to excite nuclei. This reduces the number of resonant photons within the photon flux as the beam traverses through the target. Therefore, nuclei at the beginning of the target are more likely to be excited than those deeper inside the material. This becomes a problem when needing the beam's photon flux to determine a cross section or an absolute excitation probability. If the photon flux can be found before it arrives at the target, it is often used in calculations of the two quantities mentioned above. However, since it is dependent on the distance traveled within a target, this value is often incorrect.

Here, I assess the reliability of a new, modified version of the self-absorption method called Polarized Self Absorption (PSA) by determining the full and partial widths of the well-defined 1^+ excited state at 10.71 MeV in ^{24}Mg. In Section II, I discuss the history of the self-absorption method, the advancements that inspired the PSA method, and how PSA works. In Section III, I record the derivation for the equations used in PSA, explain why ^{24}Mg was chosen for the experiment, and state any corrections that need to be accounted for before a result is obtained. The new dual-target setup for PSA is explained in Section IV. The overall process of calculating the full and partial widths of ^{24}Mg, the mass-weighted uncertainty, as well as the challenges I ran into, are detailed in Section V. In Section VI, I report the branching ratios of the 10.71 MeV state, the mass-weighted asymmetry, and the experimental asymmetry and use these results to assess the reliability of the PSA method in Section VII.

II. SELF ABSORPTION

A. Literature Review

Self absorption is another, less common, experimental method of examining excited states and was originally introduced by Franz Metzger in 1956 [7]. It consisted in carrying out two separate measurements: a normal NRF measurement and a second NRF one, but with the bremsstrahlung beam passing through an identical target before hitting the primary target for a traditional NRF measurement. By passing the beam through a second, identical absorbing target before reaching the primary NRF one, the beam will consist of fewer γ rays with resonant energies [7]. This results in fewer counts measured at resonant energies from the NRF target. Fig. 1 compares an energy spectrum of a bremsstrahlung beam before and after resonating with an absorbing target. In the approximation that
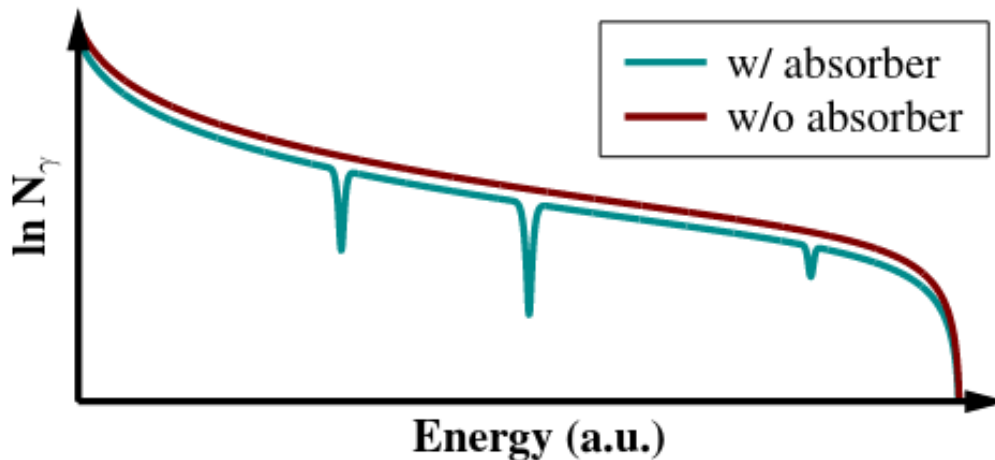
FIG. 1: Graphic which illustrates the gamma-ray energy spectrum with and without the absorbing target. Take note of how in the spectrum with the absorber, there are fewer gamma rays with energies that resonate with the primary target. Graphic from [8].

the total width is small compared to the Doppler broadening, the difference in the count rates is proportional to $\Gamma_{0\to i}$ [6]. Therefore, by comparing the two count rates, both $\Gamma_{0\to i}$ and Γ_i can be found without the knowledge of all possible decay paths from the dependency described in Eqs. 1 and 3.

There are three primary setbacks to this method. First, the detection system around the NRF target needs to be properly shielded from the scattering off the absorber target. For proper results, the shielding needs to be infeasibly perfect. Second, an absolute measurement of the photon flux of the beam between the two targets is required for calculating the elastic cross section. Third, the approximation that the total width is small compared to the Doppler broadening is not valid in most cases [6]. Regardless, the concept that Γ_i can be found from comparing the count rates of the two measurements still stands.

A modification to the original self-absorption method called Relative Self Absorption (RSA) was developed in 2015 by Christopher Romig [8]. RSA uses an additional normalization target, different from the primary one, placed between the absorbing and NRF targets to monitor the photon flux. This normalization target needs to have few excited states which do not interfere with the excited states of the original target, but also broadly cover the entire energy spectrum [8]. For example, in his investigation of ^{6}Li via RSA, C. Romig used ^{11}B as the normalization target. However, finding such a target for a bremsstrahlung beam can be quite difficult when examining isotopes with many decay cascades such as ^{24}Mg.

In 2018, Savran and Isaak proposed a modified self-absorption method using a quasi-monochromatic photon beam like the one produced at the High-Intensity Gamma-ray Source (HIγS) located at the Triangle Universities Nuclear Laboratory [9]. In comparison to a bremsstrahlung beam which contains photons covering a very large energy range, a quasi-monochromatic photon beam's energy range is narrow. For reference, the beam produced at HIγS has a full width half maximum (FWHM) of 300 keV at a beam energy of 10 MeV. Narrowing the FWHM of the photon beam drastically reduces the background, as illustrated in Fig. 2, because there are fewer photons with nonresonant energies.

Savran and Isaak also proposed a new experimental setup. In addition to the NRF and absorbing target, a third target with its own gamma-ray detection system was added before the absorber. This allowed for both measurements used in Franz Metzger's self-absorption method to be done simultaneously, halving the total experiment time [6, 9]. There are, however, some setbacks. An absolute normalization of the photon flux is still required, the additional detection system requires more, precise corrections for the relative efficiencies and dead times of the gamma-ray detectors, and the experimental setup can be difficult to assemble [6]. As of right now, Savaran and Issak have finished the first measurements and are currently analyzing data to assess the reliability of their method.
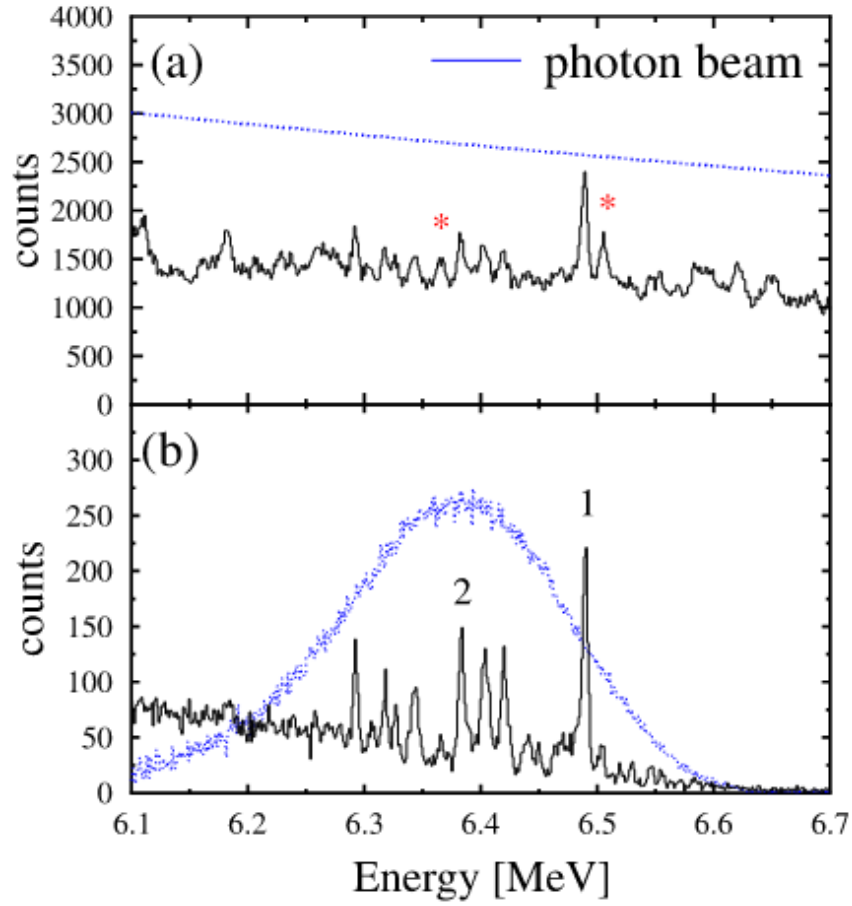
FIG. 2: Comparison of the NRF spectra of the reaction ^{128}Te(γ,γ') measured at the Darmstadt High Intensity Photon Setup using a bremsstrahlung beam (a) and a quasi-monochromatic beam (b). Take note of how the peaks in (b) are more visible due to the background being significantly reduced. The blue lines in both graphs represent the energy distribution of the incoming photon beam [9].
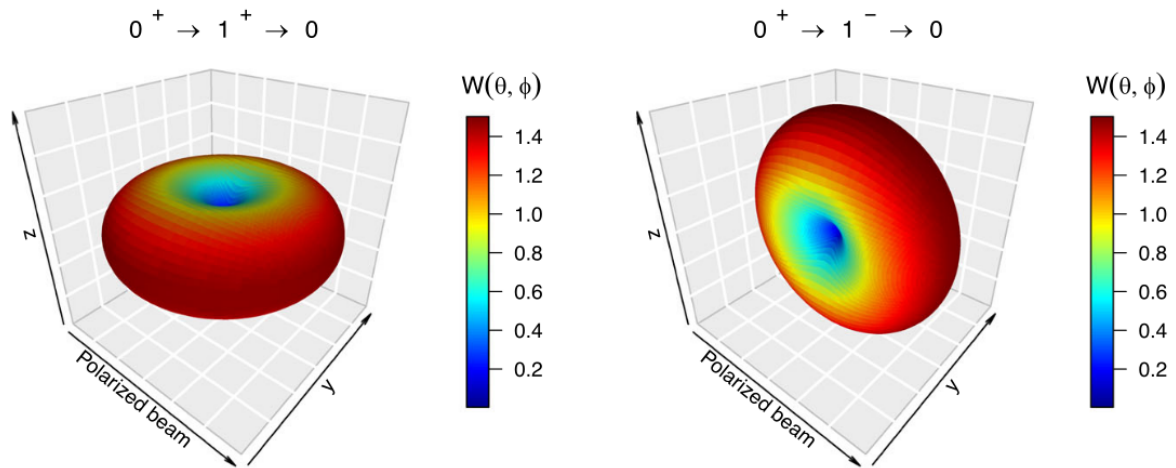

FIG. 3: 3D representation of the radiation patterns for $0 \to 1^{\pm} \to 0$ decay cascade with the polarized beam directed along the x-axis, polarized along the x-y plane. Both radiation patterns resemble a toroid [6, 10].

B.   Polarized Self Absorption

In 2021, Udo Friman-Gayer proposed the Polarized Self-Absorption method (PSA), which is a modified version of Savran and Isaak's self-absorption method. PSA takes advantage of both the quasi-monochromaticity and high degree of linear polarization of the photon beams produced at HIγS to eliminate the necessity for two gamma-ray detector systems. The linearly polarized beam allows for a definitive angular distribution for elastically scattered photons. An example of the angular distribution for the decay cascade $0^+ \to 1^\pm \to 0$ can be seen in Fig. 3. Without a perfectly linearly polarized beam, the radiation would not exhibit the angular distributions described in Ref. [10].

At HIγS, the simplest gamma-ray detector configuration is cross-like, as seen in Fig. 4. There are four well-positioned detectors around the beam: two parallel and two perpendicular to the polarization axis of the beam. This cross-like configuration allows for a maximum of the count-rate asymmetry, A, as defined in [6, 11]

$$A = \frac{N_\parallel - N_\perp}{N_\parallel + N_\perp} \tag{4}$$

in which $N_\parallel$ and $N_\perp$ are the numbers of counts detected in the parallel and perpendicular detectors, respectively. For instance, in the $0^+ \to 1^+ \to 0$ cascade seen in Fig. 3, the perpendicular detectors should see little to no emitted radiation, resulting in $A \approx 1$.

PSA's experimental setup differs from Savran and Isaak's by repositioning the two NRF targets and removing the absorber target. The first NRF target is placed at the center of the detection system, while the second is placed slightly downstream from the first. The central target is used for the first NRF measurement as well as an absorber for the downstream target. If the targets are excited to a 1^+ level which results in the decay cascade $0^+ \to 1^+ \to 0$, the radiation pattern shown in Fig. 3 will be present. At the first, central, target, the perpendicular detectors will not observe γ rays. They will, however, observe γ rays from the second, downstream target. In contrast, the parallel detectors detect radiation emitted from both targets. This is depicted in Fig. 5. The foundation of the PSA method relies on the two targets having different count-rate asymmetries to distinguish between them. The placement of the targets in Fig. 5 indicates the central target's count-rate asymmetry is 1, while the downstream target's count-rate asymmetry is much lower.

The experimental effective asymmetry, $\bar{A}_{Ex}$, when both targets are present, is given by

$$\bar{A}_{Ex} = \frac{(N_\parallel^c + N_\parallel^d) - (N_\perp^c + N_\perp^d)}{(N_\parallel^c + N_\parallel^d) + (N_\perp^c + N_\perp^d)} \tag{5}$$

where N_p^τ is the number of counts observed by a parallel detector, $p = \parallel$, or perpendicular detector, $p = \perp$, for the central target, $\tau = c$, or downstream target, $\tau = d$ [12]. Via Monte-Carlo simulations, a run in which only the central target is present, and a run in which both targets are present, an effective asymmetry, $\bar{A}$ can be calculated which is dependent on the total width Γ_i of the observed decay. By equating the asymmetries and using a root finder, Γ_i can be found without knowledge of all decays from an excited state.

There are a few advantages of the PSA method over the traditional self-absorption and Savraan and Isaak's method. Compared to the traditional self-absorption method, time is greatly reduced as both the NRF and absorber measurements are done together rather than individually. Compared to the Savran and Isaak's method, the use of only one detection system means it is easier to setup and align. As stated by U. Friman-Gayer, the compactness of the system reduces the "spreading of the transversal beam profile between the two targets to a negligible amount" [6]. Since both measurements are done in one detection system, strong shielding is also not required. The biggest disadvantage of the PSA method is that it has limited usefulness in odd-even and odd-odd nuclei. The non-zero ground state results in emission with more complex angular distribution patterns, reducing the asymmetry of the cascade(s) of interest. As a result, considerably longer run times are needed to properly distinguish the origin of the
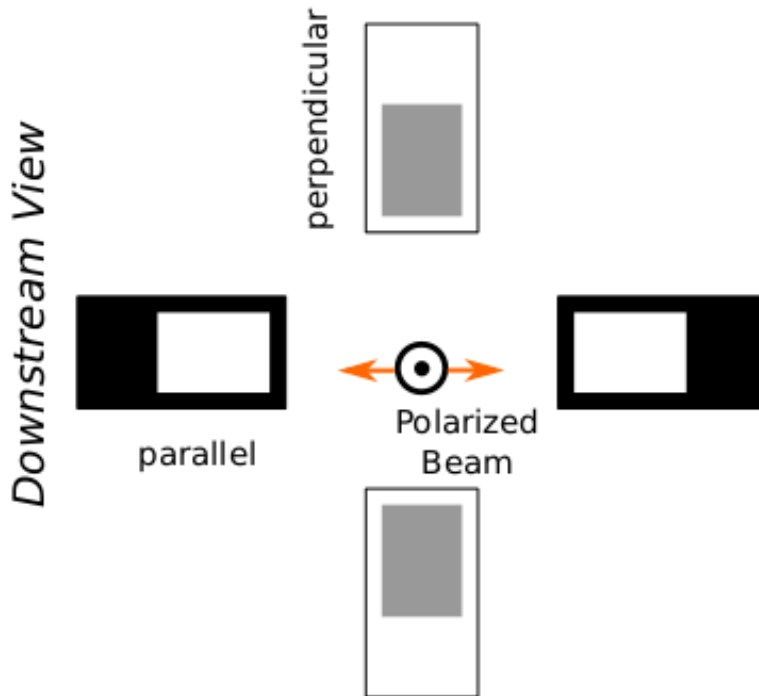
FIG. 4: Depiction of the cross-like detector configuration. The polarized beam is coming out of the page, with its polarization indicated the orange arrows. The parallel detectors as shaded black and white, while the perpendicular detectors are shaded white and gray. [6]

emitted photons.

III.   THEORY

A.   Why ^{24}Mg?

I used ^{24}Mg to show the strengths and effectiveness of the PSA method. Current knowledge of the low-spin resonances of ^{24}Mg is poor, with uncertainties for the full and partial widths being up to 20%. These large uncertainties are a result of the many significant decay branches found in ^{24}Mg which complicate the determination of Γ_i and the photoabsorption cross section when probed with NRF [6, 13]. As stated above, this complication can be bypassed using the PSA method.

In most photon-scattering experiments, ^{11}B is used as the standard photon-flux calibration. The large decay widths, the few strong dexcitations distributed over a wide energy range, and the reliable knowledge of the multipole mixing ratios all make ^{11}B a strong calibration standard [14, 15]. In addition, its high natural abundance of 80.1% makes ^{11}B the industry standard for NRF measurements [6, 16].

Although ^{11}B is most-commonly used for photon-flux calibrations, physicists are always looking for new calibration standards to refine their measurements. In particular, ^{24}Mg has been identified as a promising calibration on par with ^{11}B for multiple reasons. It has a few, well-spaced, strong $1^{\pm}$ resonances at high energies up to the proton separation energy of 11.7 MeV. It has a low proton number, indicating minimal nonresonant scattering. Finally, it has a high natural abundance of 78.99%, making it a prime candidate for a new calibration standard [6, 16]. Despite its promise, little is known of ^{24}Mg's high-energy, low-spin resonances due to these states having strong, many-state decay cascades that are often overlooked or hard to characterize due to background.

This effect can be seen in the discrepancy of recorded decay cascades between the ENSDF data sheets [17] and
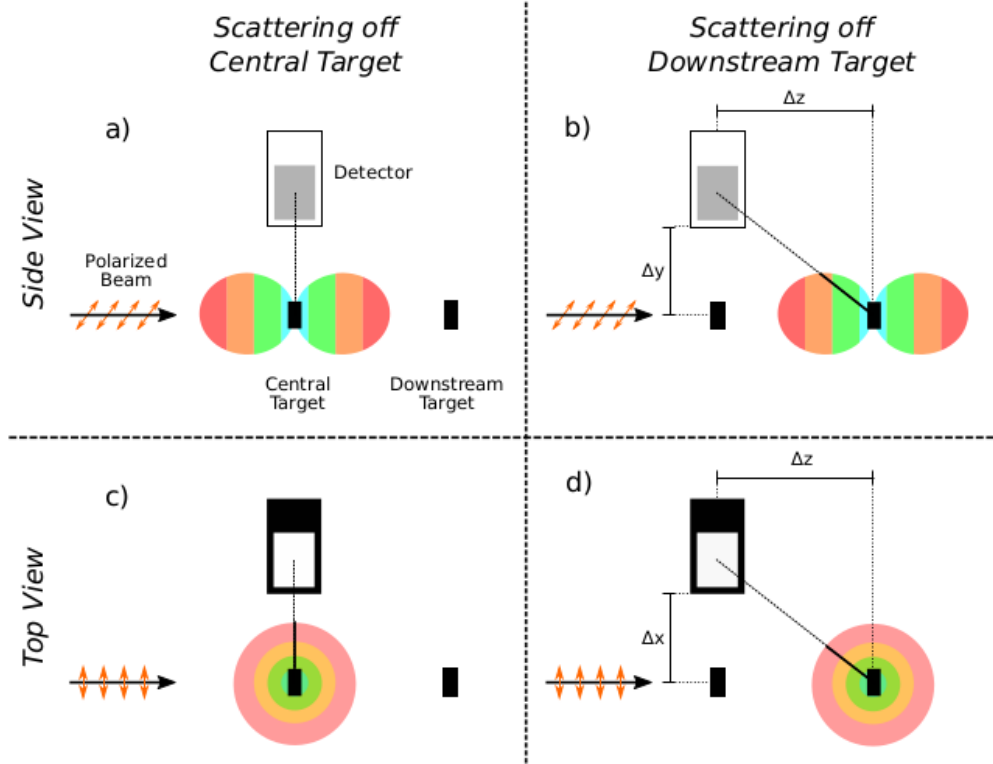
FIG. 5: Depiction of the polarized self absorption principle. Sections a) and b) depict a side view of the configuration and the targets' interactions with a perpendicular detector. Sections c) and d) depict a top view of the configuration and the targets' interactions with a parallel detector. The central target is placed at the center of the detector configuration, Δx and Δy away from the parallel and perpendicular detectors, respectively. The downstream target is placed a distance Δz downstream from the central target. The beam is incoming from the left, with its polarization indicated by the orange arrows. As seen in a) and b), the perpendicular target should only detect emission from the downstream target. Sections c) and d) depict the parallel detector detecting emissions from both the central and downstream targets. [6]

an investigation done by J. Deary et al. [18]. For the 1^+ excited state at 10.71 MeV, Wang et al. lists no other decay branch other than to the ground state [17]. However, [18] lists four other decay paths with relative intensities of $19.9\%, 2.4\%, 0.9\%$, and 0.6% relative to the ground state decay [18].

A MgO target was used due to its well-known phonon density of states [6, 19]. Since the PSA method depends on the resonance width of excited states, a nucleus' motion within the atomic lattice structure must be considered as a correction [6, 20, 21]. As stated in [6], this can be done with the Debeye approximation; unfortunately, it is challenging to use when working with a highly reactive material such as ^{24}Mg. However, the Debeye approximation can be bypassed by using the phonon density of states to calculate the resonance broadening [22]. Due to MgO being both readily available and having a well-known phonon density of states, it was chosen as the target for this experiment.

B. Mass-weighted Asymmetry

To establish that self absorption is taking place within the experiment, the mass-weighted asymmetry is used:

$$\bar{A}_{MW} = \frac{m_c \times \bar{A}_{Ex,c} + m_d \times \bar{A}_{Ex,d} \times \epsilon_{corr}}{m_c + m_d \times \epsilon_{corr}} \tag{6}$$

TABLE I: Definitions of variables used in the text

Variable	Definition
$N_{p,\text{sim}}^{\tau}$	number of simulated counts with a target in position τ and detector p with isotropic emission
$N_{p,\text{sim},w}^{\tau}$	number of simulated counts, with angular correlation effects, with a target in position τ and detector p
Δt^{τ}	live time of the measurement for target in position τ
$N_p^{\tau,\tau}$	number of counts of a given decay for a target in position τ and detector p
$\langle \Phi^{\tau} \sigma \rho_A^{\tau} \rangle$	the integral of the resonance absorption density, over the spatial extent of the target, symbolized by the product of the normalized photon flux Φ^{τ} at the target position τ, the scattering cross section σ, and the areal density of the target ρ_A^{τ} with a target area A

in which m_{τ} is the mass of the target in position τ, which corresponds $\tau = c$ for a target in the central position and $\tau = d$ for the downstream, while $\bar{A}_{ex,\tau}$ is the experimental asymmetry when just the target in position τ is present, ϵ_{corr} is the correction for the difference in efficiencies of the downstream and upstream targets given as:

$$\epsilon_{corr} = \frac{N_d \times \Delta t^c}{N_c \times \Delta t^d} \tag{7}$$

in which N_{τ} is the number of counts recorded when just the target in position τ is present, and δt^{τ} is the live time of the measurement for when just target τ is present.

Without the central target, there is no absorption of the photon beam before it reaches the downstream one. This would result in more counts being detected from the downstream target; consequently, A_d is weighed more in Eq. 6 as compared to Eq. 5. Therefore, a difference in the asymmetries for Eq. 6 and Eq. 5 would show that self absorption is truly taking place and PSA has practical potential.

C. Effective Asymmetry

In this experiment, the primary observable is the effective count-rate asymmetry. The equation below is a result of a derivation given to me in a private communication by Udo Friman-Gayer [12]:

$$\bar{A}_{eff} = \frac{\left(\langle \Phi^c \sigma \rho_A^c \rangle + \frac{N_{\parallel,\text{sim},w}^d}{N_{\parallel,\text{sim}}^d} \frac{N_{\parallel,\text{sim}}^c}{N_{\parallel,\text{sim},w}^c} \frac{N_{\parallel,\text{cal}}^d \Delta t^c}{N_{\parallel,\text{cal}}^c \Delta t^d} \langle \Phi^d \sigma \rho_A^d \rangle \right) - \left(\frac{N_{\perp}^{c,c}}{N_{\parallel}^{c,c}} \langle \Phi^c \sigma \rho_A^c \rangle + \frac{N_{\perp}^{c,c}}{N_{\parallel}^{c,c}} \frac{N_{\perp,\text{sim},w}^d}{N_{\perp,\text{sim}}^d} \frac{N_{\perp,\text{sim}}^c}{N_{\perp,\text{sim},w}^c} \frac{N_{\perp,\text{cal}}^d \Delta t^c}{N_{\perp,\text{cal}}^c \Delta t^d} \langle \Phi^d \sigma \rho_A^d \rangle \right)}{\left(\langle \Phi^c \sigma \rho_A^c \rangle + \frac{N_{\parallel,\text{sim},w}^d}{N_{\parallel,\text{sim}}^d} \frac{N_{\parallel,\text{sim}}^c}{N_{\parallel,\text{sim},w}^c} \frac{N_{\parallel,\text{cal}}^d \Delta t^c}{N_{\parallel,\text{cal}}^c \Delta t^d} \langle \Phi^d \sigma \rho_A^d \rangle \right) + \left(\frac{N_{\perp}^{c,c}}{N_{\parallel}^{c,c}} \langle \Phi^c \sigma \rho_A^c \rangle + \frac{N_{\perp}^{c,c}}{N_{\parallel}^{c,c}} \frac{N_{\perp,\text{sim},w}^d}{N_{\perp,\text{sim}}^d} \frac{N_{\perp,\text{sim}}^c}{N_{\perp,\text{sim},w}^c} \frac{N_{\perp,\text{cal}}^d \Delta t^c}{N_{\perp,\text{cal}}^c \Delta t^d} \langle \Phi^d \sigma \rho_A^d \rangle \right)} \tag{8}$$

for which the variable definitions are given in Table I.

The simulated count rates, $N_{p,\text{sim}}^{\tau}$ and $N_{p,\text{sim},w}^{\tau}$ are found with the GEANT4 simulation software, which uses Monte Carlo methods to simulate radioactive decay. The live time of the measurements, Δt^{τ}, is related to how long those respective measurements take, and can be found by looking through a log of prior experiments. The number of counts of a given decay, $N_p^{\tau,\tau}$, is found with calibration measurements with isotropic emission for the efficiency, and $N_{\parallel}^c + N_{\parallel}^d$ is found with measurements of targets in both the central, (c), and downstream, (d), positions.

The resonance absorption density, as defined by the supplemental materials in [6, 22]:

$$\alpha_{0 \to x, \tau}(E, z_\tau, {}^A_Z X) \approx \tilde{\sigma}_{0 \to x, \tau}(E, {}^A_Z X) \frac{\Phi(E, z_\tau)}{\Phi(E, 0)} \tag{9}$$

where Φ is the photon flux, z_τ is the distance into the target, and $\tilde{\sigma}(E; \Gamma_{i \to 0}, \Gamma_i, T_{\text{eff}})$ is the Doppler-broadened cross section. In Ref. [22], the scattering cross section σ is used rather than $\tilde{\sigma}$, this is because using $\tilde{\sigma}$ corrects for the thermal motion of a nuclei in an atomic lattice.

The photon flux, given in the supplemental materials in [6, 22], is:

$$\Phi(E, z) = \Phi(E, 0) e^{-[\mu_\tau(E) + \tilde{\sigma}_{0 \to i}(E; {}^A_Z X) n_\tau({}^A_Z X)] z} \tag{10}$$

in which μ_τ is the nonresonant attenuation coefficient for MgO for target τ:

$$\mu_\tau(E) = \frac{m_{a, \text{Mg}}}{m_{a, \text{Mg}} + m_{a, \text{O}}} \mu_{\text{Mg}}(E) + \frac{m_{a, \text{O}}}{m_{a, \text{Mg}} + m_{a, \text{O}}} \mu_{\text{O}}(E) \tag{11}$$

where $m_{a, X}$ is the atomic mass of element X and μ_X is the x-ray attenuation coefficient for element X found in the Ries python package created by Udo Friman-Gayer [23]. n_t is the mass distribution inside the nucleus given by

$$n_\tau = n_{\text{Mg}} c_{24\text{Mg}} c_{\text{MgO}} \tag{12}$$

in which n_{Mg} is the fraction of magnesium atoms in MgO, $c_{24\text{Mg}}$ is the enrichment of ^{24}Mg in MgO, and c_{MgO} is the enrichment of MgO in the magnesia.

By inputting Eq. 10 into Eq. 9 and analytically taking the spatial integral over z,

$$\langle \Phi^\tau \sigma \rho_A^\tau \rangle = \int \frac{\tilde{\sigma}_{0 \to i}}{\mu_\tau(E) + \tilde{\sigma}_{0 \to i}(E; {}^A_Z X) n_\tau({}^A_Z X)} \times (1 - e^{-[\mu_\tau(E_x) + \tilde{\sigma}_{0 \to i}(E; {}^A_Z X) n_\tau({}^A_Z X)] \rho_A^\tau}) dE \tag{13}$$

where ρ_A^τ is the areal density of target τ.

In total, calculating $\langle \Phi^c \sigma \rho_A^\tau \rangle$ requires knowledge of the:

- areal densities, ρ_A^τ of both targets, given by the measurable mass m^τ divided by the target areas A^τ
- enrichment, c_{MgO}, of the target material in magnesia
- enrichment, $c_{24\text{Mg}}$, of the target material in ^{24}Mg
- mass attenuation coefficient of μ of magnesia
- effective temperature T_{eff} of magnesia
- mass $m_{24\text{Mg}}$ of the isotope of interest
- excitation energy E_x of the state of interest
- ground-state branching ratio Γ_0/Γ
- total width Γ

The calculation of $\langle \Phi^c \sigma \rho_A^\tau \rangle$ requires prior knowledge of both Γ_0/Γ and Γ, which, at first glance, appears to contradict the purpose of the PSA to find the total width without prior knowledge. However, by using the quasi-monochromaticity of the photon beam at HIγS, a good estimate of the ground-state branching ratio can be found. Therefore, by equating Eq.'s 4 and 8, a root finder can be used to obtain the total width.

The additional measurement required to find an estimate of the ground state branching ratio does slightly offset the time benefit of using PSA. However, for isotopes in which the ground state branching ratio is well known, this additional run is not required and can still be used to find a proper value for Γ.

TABLE II: High-Purity Germanium Detector Positions

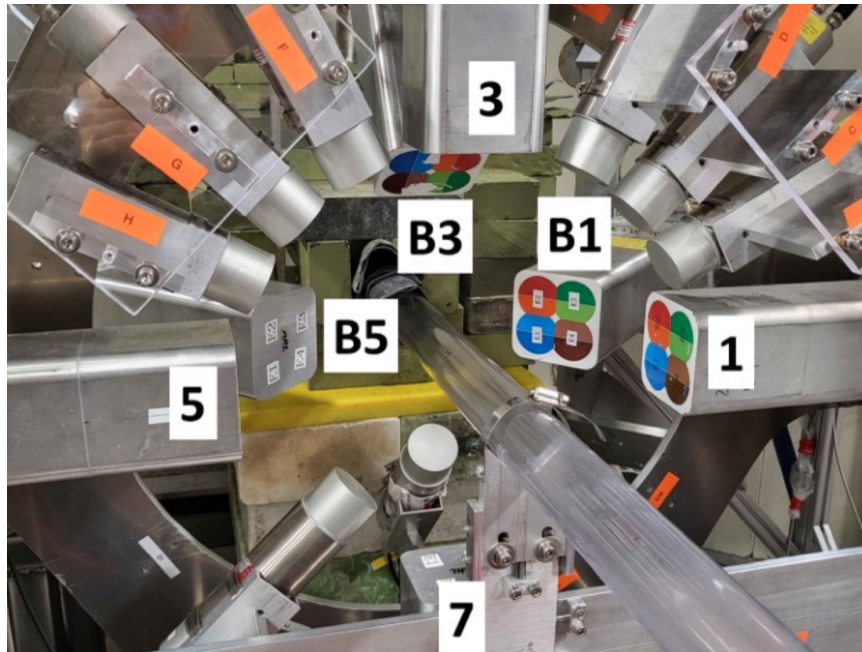| Detector	Type	θ	ϕ	Distance (inch)
1	Clover HPGe	90°	0°	8.0 ± 0.0625
3	Clover HPGe	90°	90°	7.9375 ± 0.0625
5	Clover HPGe	90°	180°	8.0625 ± 0.0625
7	Clover HPGe	90°	270°	8.0 ± 0.0625

FIG. 6: Picture of the clover-array setup for this experiment. All detectors are labeled. There are three additional HPGe detectors in the picture; these were present during the experiment, but were not used in the analysis. Photo courtesy of David Gribble.

IV. EXPERIMENTAL SETUP

A. The Clover Array

The clover-array setup consisted of eight high-purity Germanium detectors, of which I only used the four surrounding the beam in a cross-like configuration as in Fig. 4. Each of the detectors is equipped with four crystals arranged in the cryostat as seen in Fig. 6. Detector 1 is an exception, as one of its crystals was not working at the time of the experiment. These detectors and their positions are described in Table II. The four detectors were of the high-purity Germanium type. They had absorbers on them so to not overwhelm the crystals with too many γ rays of low energy. In total, one 0.04 inch Cu, one 0.08 inch Cu, one 0.0450 Pb, and one 0.100 inch Pb filter were placed on each detector. The other, unused, high-purity Germanium detectors were placed at backwards angles. The physical clover configuration can be seen in Fig. 6.

B. Dual-Target Configuration

The dual-target configuration of PSA is presented in Fig. 7. When determining a proper distance between the targets, two components were considered. As the distance between the targets increases, the effective asymmetry for the downstream target decreases, which is the desired effect. However, this also means the detectors will detect fewer
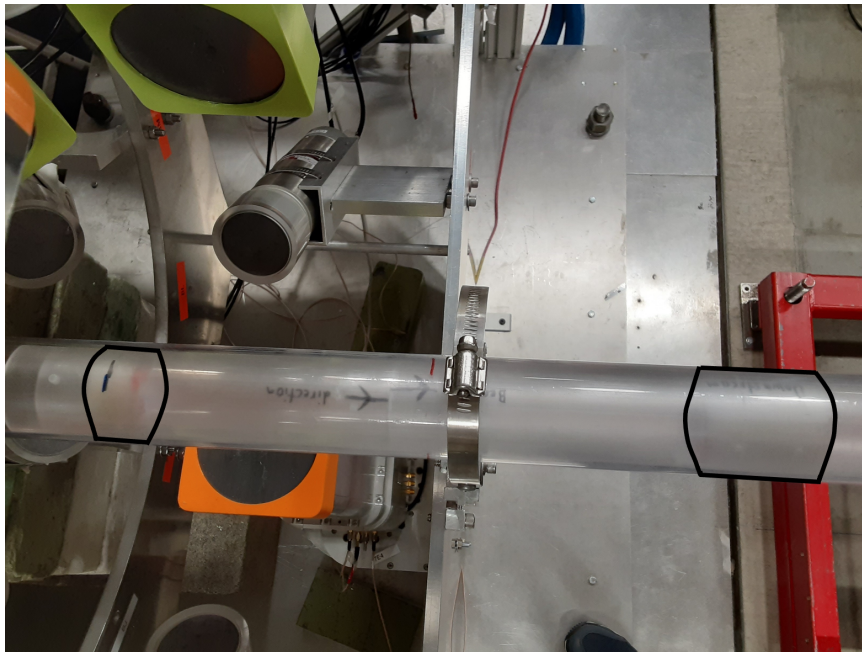
FIG. 7: Top-down view of the dual-target pipe setup. Both targets are outlined in black, with the central target being on the left. Photo courtesy of Udo Friman-Gayer.

γ ray emissions from the downstream target. A distance of 11.75 inch was chosen as a good compromise between effective asymmetry and radiation detected from the downstream target [6].

The MgO targets were contained within polyethylene cylindrical target capsules with an inner radius of 0.5 inch. A diagram of the capsule can be found in Fig. 8. The radius was chosen such that it would be larger than the collimator radius of 0.375 inch. Doing so ensured the beam would not hit the container walls, only the end caps and the MgO target. Note that, the downstream target was larger than the central target to compensate for the lower detector efficiency due to the larger source-crystal distance [6]. Thus, the downstream target was chosen to be about twice as long as the central target. The central target had a mass of $16.3691 \pm 3 \times 10^{-4}$ g and the downstream one had a mass of $38.5734 \pm 3 \times 10^{-4}$ g. Finally, to ensure a safe vacuum a 1.0 mm diameter hole was drilled into both capsules.

V. METHODS

I analyzed data from 7 sets of runs. These runs, their target configurations, and their run times are listed in Table III. Going forward, the target configuration of each run will be referenced as Central Target + Downstream Target. If one of the positions was empty for a given run, it is listed as 'Nothing.' There were two sets of runs involving MgO with the beam at 10.71 MeV: a run in which only the central target was present, and another with both the central and downstream targets present. There were three sets of calibration runs that used a radioactive source with isotropic emission in the central target position. Those sources were ^{56}Co, ^{152}Eu, and a mixed source provided by HIγS.

A. Fitting ^{24}Mg Transitions

For a given run, each γ-ray detector developed a histogram of the number of counts detected per energy. If a given nucleus experiences a decay of energy E_γ, there will be a Gaussian peak at E_γ in the resultant histogram. I fit these peaks by loading the resultant histograms into the nuclear spectrum analysis software HDTV. In HDTV, I
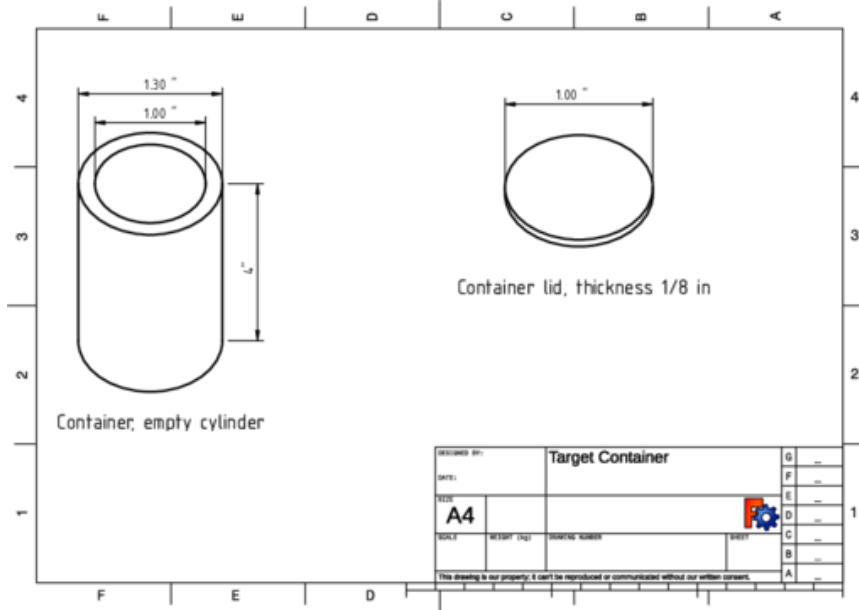
FIG. 8: Diagram of the target container used to hold the MgO target.

can specify the region of which there is a peak, a sample of background radiation, and the location peak's centroid to fit a Gaussian curve. By fitting a Gaussian to these peaks, I can determine their position, area, and width. Within my resultant spectra, there were many peaks that were not from ^{24}Mg. The impure MgO target resulted in peaks that belonged to other isotopes such as ^{26}Mg. Thankfully, a prior Research Experiences for Undergraduates (REU) student, Arlee Shelby, had told me in a private communication that she already determined the origin of the peaks and calibrated the spectra [24]. As in Ref. [18] of J. Deary et. al., Arlee had found four more decay branches from the 10.71 MeV state as shown in Fig. 9. Thanks to Arlee, I saved time by focusing my efforts on fitting only ^{24}Mg decay peaks.

Before I began fitting ^{24}Mg peaks for the so-called MgO + Nothing runs, I found that there was a problem in some of the runs involving MgO in which germanium crystal 2 in detector 1 had gain problems, resulting in poor γ-ray energy identification. This problem can be seen in Fig. 10 where gain shifts result in double-peaking. As a result, I was unable to properly fit a Gaussian to the parallel detectors' summed spectra. Instead, I used the integrate function within HDTV, the nuclear spectra analysis software I used, to find the area of these peaks. This was only found for the runs with MgO. The integration function relies heavily on properly identifying background radiation, a small error could easily change the reported value. As a result, I did not use this feature for the spectra from the perpendicular detectors.

Fitting peaks within the perpendicular detectors' spectra became a problem when working with low intensity peaks.

TABLE III: Runs analyzed in this work. Column 1 states the target arrangement. Column 2 shows the energy of the beam for a given run; if no beam was used it is listed as 'Radioactive Decay.' Column 3 lists the runtimes.

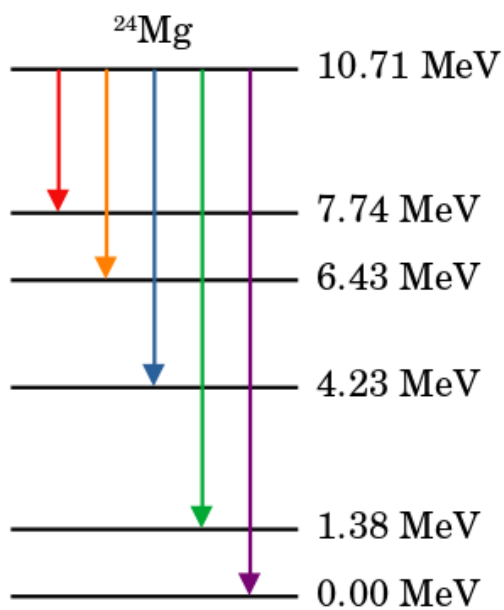| Target 1 + Target 2	Energy (MeV)	Runtime
MgO + Nothing	10.71	6 Hours 36 Min.
MgO + MgO	10.71	9 Hours 8 Min.
Nothing + MgO	10.71	7 Hours 20 Min.
^{56}Co + Nothing	Radioactive Decay	32 Hours 23 Min.
^{152}Eu + Nothing	Radioactive Decay	17 Hours 20 Min.
Nothing + ^{152}Eu	Radioactive Decay	14 Hours 46 Min.
Mixed Source + Nothing	Radioactive Decay	16 Hours 44 Min.

FIG. 9: Diagram of the decay branches from the 10.71 MeV state in ^{24}Mg.
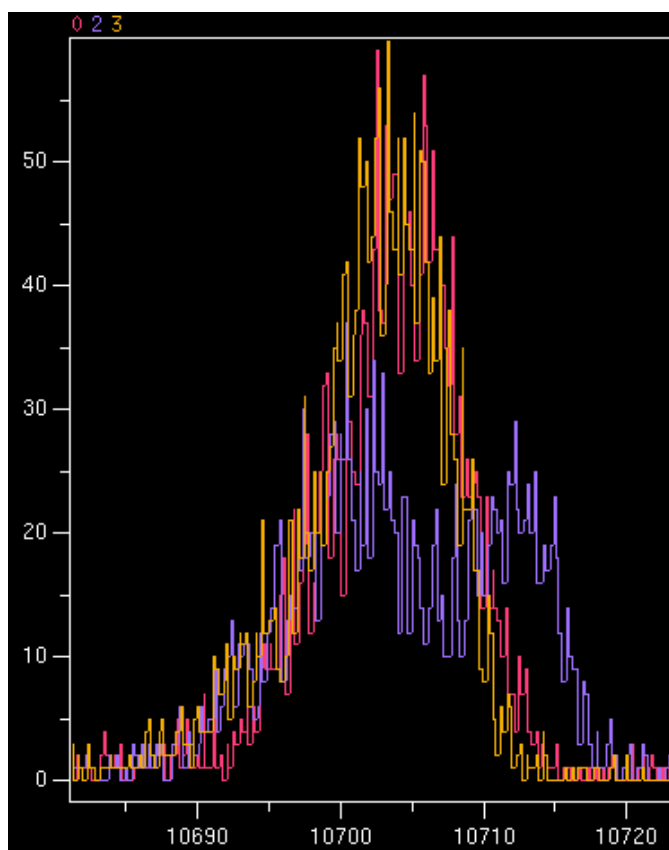

FIG. 10: The 10.71 MeV peak for crystals 0, 2, and 3 in detector 1. Crystals 0, 2, and 3 correspond to the red, purple, and yellow histograms respectively. The double peaking from crystal 2 was due to a problem in the gain factor, and is found in every peak from this crystal.
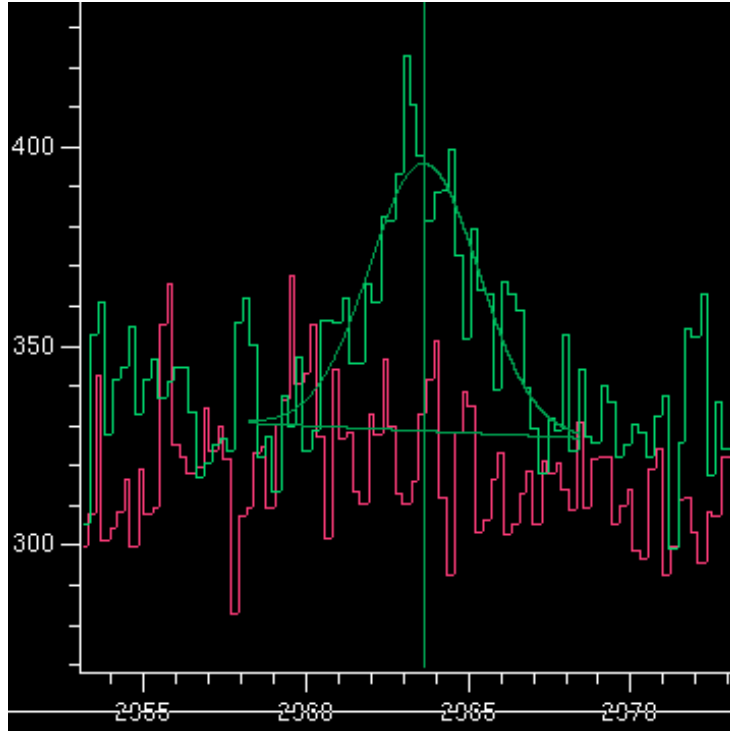
FIG. 11: The $E_\gamma = 2964$ keV decay peak for the parallel detectors, red histogram, and perpendicular detectors, green histogram. Due to the transition's strong angular distribution, the parallel detectors see practically no peak.

However unlikely, randomized nonresonant scattering can result in peaks appearing in spectra and can lead physicists to wrongly believe that there is a decay with a specific energy when there is not. As a result, it is said that if the uncertainty of the peak's area is around 1/3 of the area, then the peak is due to statistical chance and not a real decay.

This was not a problem for Arlee. When she had determined which peaks in the spectra were from ^{24}Mg, she did so from spectra summed up from seven detectors, meaning peaks of low intensity could still be identified. However, because I used spectra from only two detectors at a time, those low-intensity peaks were sometimes not visible either due to few counts or to the decay's angular distribution providing few counts in a certain direction, resulting in a poor Gaussian fit with large uncertainties. For example, a comparison of the $E_\gamma = 2964$ keV peak in both the parallel and perpendicular detectors' spectra can be found in Fig. 11. This decay's angular distribution did not provide enough γ rays to be seen amongst the background radiation in the parallel detectors. Another example is in Fig. 12, where the $E_\gamma = 4277$ keV peak in the perpendicular detectors' spectra is practically nonexistent due to the associate angular distribution. A Gaussian fit resulted in a nonphysical volume of -28 ± 15. To achieve a proper fit, width manipulation was used.

For a given spectra, as decay peaks increase in energy, their width, σ_w, also increases by the formula:

$$\sigma_w = \sqrt{A + B \times E_\gamma + C \times E_\gamma^2} \tag{14}$$

in which A, B, and C are parameters depending on the specific detector. To find these parameters, I fit well-defined peaks in the spectra, consisting of both background and ^{24}Mg peaks, and fit their widths to Eq. 14. Figure 13 shows the resultant fits of Eq. 14 for the perpendicular detectors.

While fitting a Gaussian is useful in finding the yield for peaks from the MgO + Nothing runs, the same could not be done for MgO + MgO ones. This is because of the Doppler shift of the emitted gamma rays from the downstream target. This resulted in a widening of the peaks, and in some instances, a double-peaked decay. Figure 14 provides a
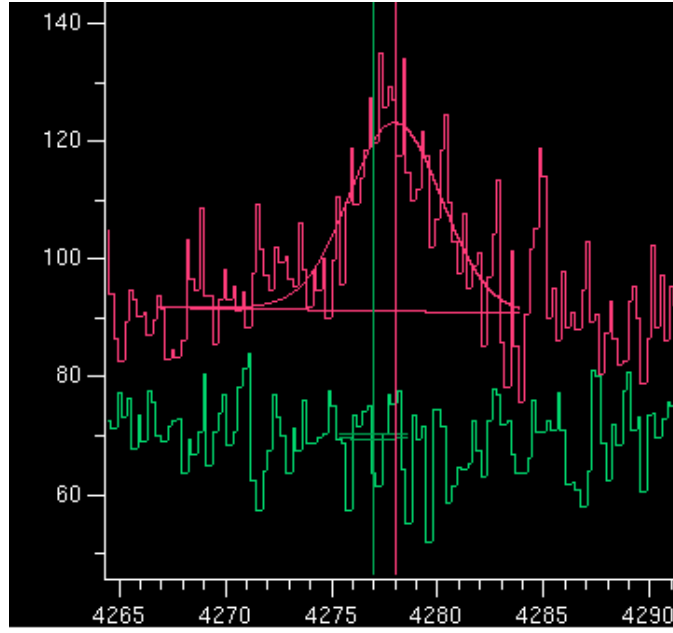
FIG. 12: The $E_\gamma = 4277$ keV decay peak for the parallel detectors, red histogram, and perpendicular detectors, green histogram. Due to the transition's strong angular distribution, the perpendicular detectors see practically no peak.
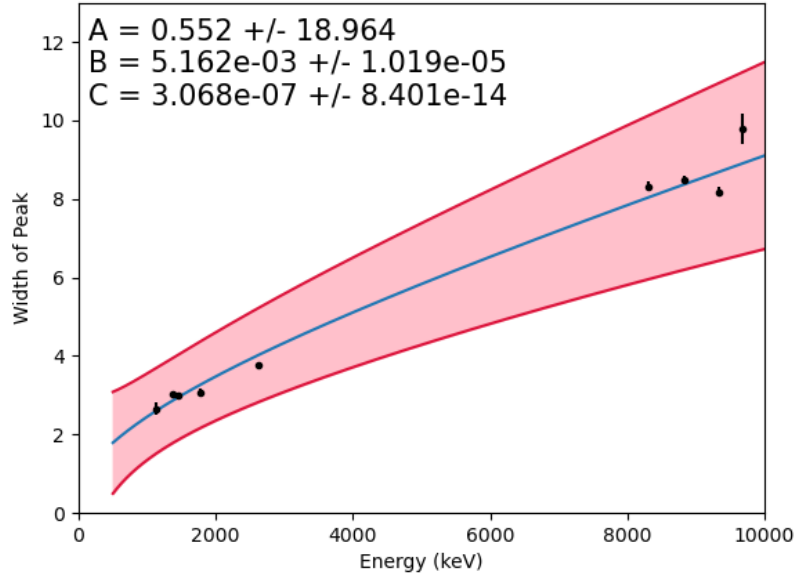

FIG. 13: Fit of Eq. 14 for strong γ ray peaks in the perpendicular detectors, 3 and 7. The coefficients and their uncertainties are listed in the top left corner. The blue line is the fit and the red signifies the area of uncertainty. Only peaks with well-defined widths were used. Other than the 1368-keV γ ray, all others with $E_\gamma < 3000$ keV are background lines.

comparison of the $E_\gamma = 9336$ keV decay peak with just the central target present and when both targets are present. As a result, the yield of these peaks was also found using the integrate function in HDTV.
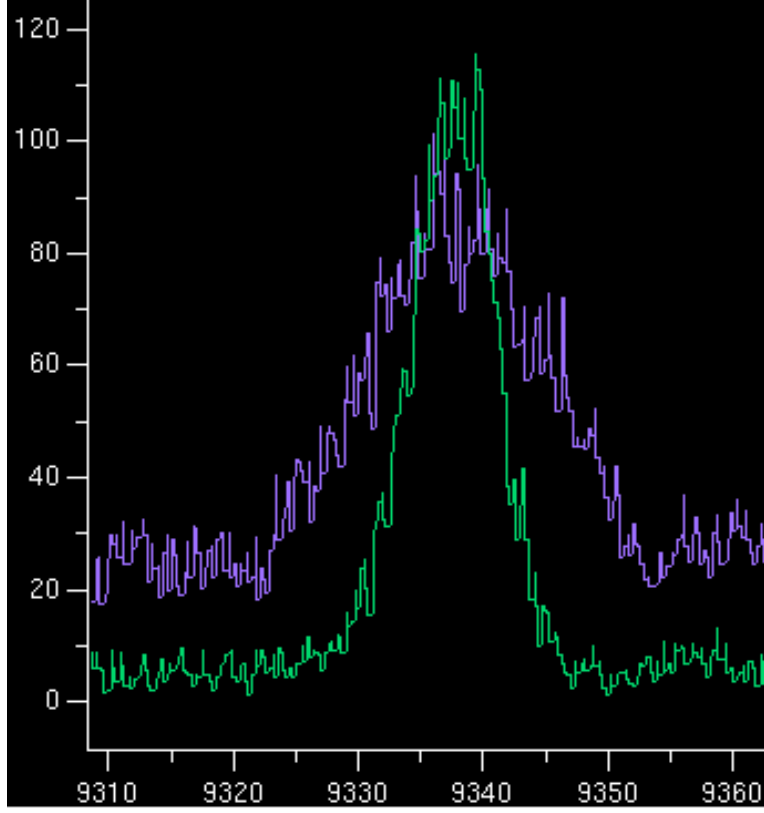
FIG. 14: Comparison of the $E_\gamma = 9336$ keV peak in the perpendicular detectors' spectra when the central target is present, green histogram, and with both targets, purple histogram. When both targets are present, there is an obvious widening of the decay peak due to a Doppler shift in the γ-ray energy for transitions from the downstream target.

B. Detector Efficiencies

A γ-ray detector is not going to be perfect; it will allow some γ rays to pass through it without detection or will only collect partial information. A detector's efficiency at a given energy is used to compensate for this properly. At the most basic level, a detector's efficiency, ϵ, for an isotropic source is:

$$\epsilon = N_i/I_i \tag{15}$$

in which N_i is the number of counts detected for decay i, and I_i is the intensity of decay i. A detector's efficiency depends on the energy of the incoming γ ray, with the relationship:

$$\epsilon(E_\gamma) = (A/E_\gamma + B \times E_\gamma)e^{C/E_\gamma + D \times E_\gamma} \tag{16}$$

in which $A, B, C,$ and D are parameters for a given detector [25]. By measuring isotropic radioactive decay from calibration sources with known intensities, an efficiency curve for a detector can be fit to Eq. 16.

To find the detectors' efficiencies, three calibration sources were used: ^{56}Co, ^{152}Eu, and a mixed source commonly used at HIγS. These radioactive sources were placed in the central target position and allowed the detectors to measure isotropic emission. Originally, only the ^{56}Co was going to be used for these calibrations due to it having many transitions up to about 3400 keV. Unfortunately, the source was weak. According to the Nuclear Data Sheets, ^{56}Co has a half life 77.236 days, but the source was used 894 days after it was made, resulting in the transitions being of very low intensity. In some instances, the peaks were too close to a background peak and the two became indistinguishable from each other. As a result, the ^{152}Eu and mixed source calibrations were also used for determining
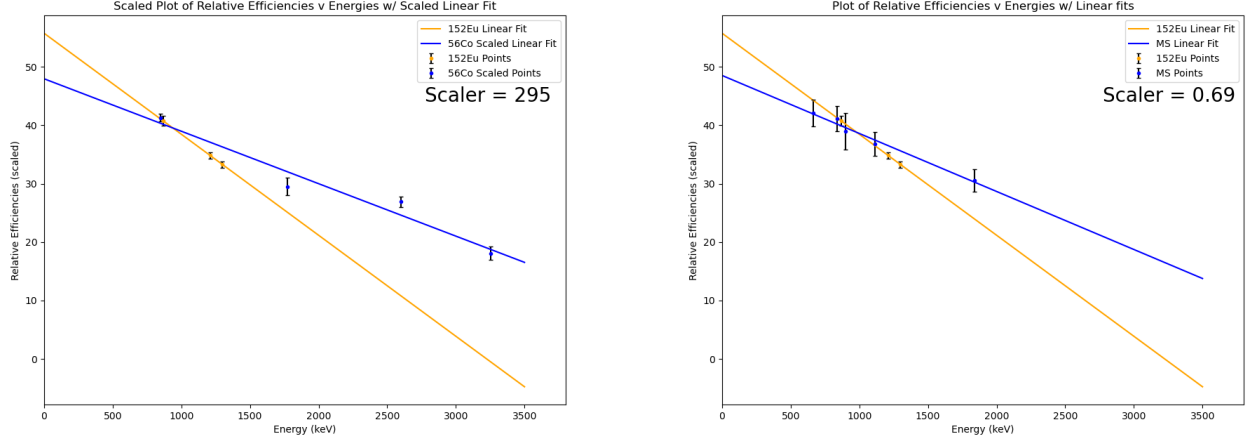
FIG. 15: Linear fits were applied to relative efficiencies, for the parallel detectors, above 800 keV. ^{56}Co and mixed source were scaled such that their linear fit would cross the ^{152}Eu linear fit at 1000 keV. The ^{56}Co was scaled up by 295 (left). The mixed source target was scaled down by 0.69 (right).

the efficiency curves. Unfortunately, the ^{152}Eu source does not have any transitions with γ rays above 1500 keV, and the mixed source only has one transition above 1200 keV, making it difficult to fit an expression such as Eq. 16 above these energies.

Using multiple calibration sources for efficiency curves is not desirable as efficiency is dependent on the absolute intensity of each source. Which is relative to the most intense decay for a given isotope. Unfortunately, in our application, only relative intensities were known for the three sources. For example, while a decay from ^{56}Co may give a relative efficiency of 0.5, a decay from ^{152}Eu may give a relative efficiency of 50. Both are true relative to that isotope's most intense decay, but fail to reflect the true nature of the detector when compared.

To compensate, I scaled the ^{56}Co and mixed source relative efficiencies to ^{152}Eu. Above about 800 keV, the efficiencies follow a somewhat linear trend. I fit a line through the points above this energy for three sources. To determine the scaling factor for the ^{56}Co and mixed source relative efficiencies, I scaled the points such that the ^{56}Co and mixed source lines would cross the ^{152}Eu line at 1000 keV. This process can be seen in Fig. 15.

The resultant relative efficiency curves for both the parallel and perpendicular detectors can be found in Fig. 16. Obviously, the overall fit by Eq. 16 is very poor. This is due to having only a few data points available in the high energy region, a poor model for the relative efficiency dependence on energy, and using three calibration sources rather than one.

To lower the uncertainty, I needed a better model to fit the efficiency of the detectors. My advisor, Dr. Janssens, informed me of how RADWARE, a software package developed for γ-ray spectroscopy over many years, had found the efficiency to be best modeled by:

$$\epsilon(E_\gamma) = \text{EXP}[(A + B \times x + C \times x^2)^{-G} + (D + E \times y + F \times y^2)^{-G}]^{-1/G} \tag{17}$$

in which $x = \log(E_\gamma/100 \text{ keV})$, $y = \log(E_\gamma/1000 \text{ keV})$, while A, B, C, D, E, F, and G are parameters specific to a detector [26]. RADWARE suggested $C = 0$ and that G be between 1 and 20 depending on how sharp the initial rise in efficiency at low energy is. After some trial and error, I found that $G = 12.5$ resulted in the best fit for both the parallel and perpendicular detectors. The new efficiency curves fit to Eq. 17 can be seen in Fig. 17.
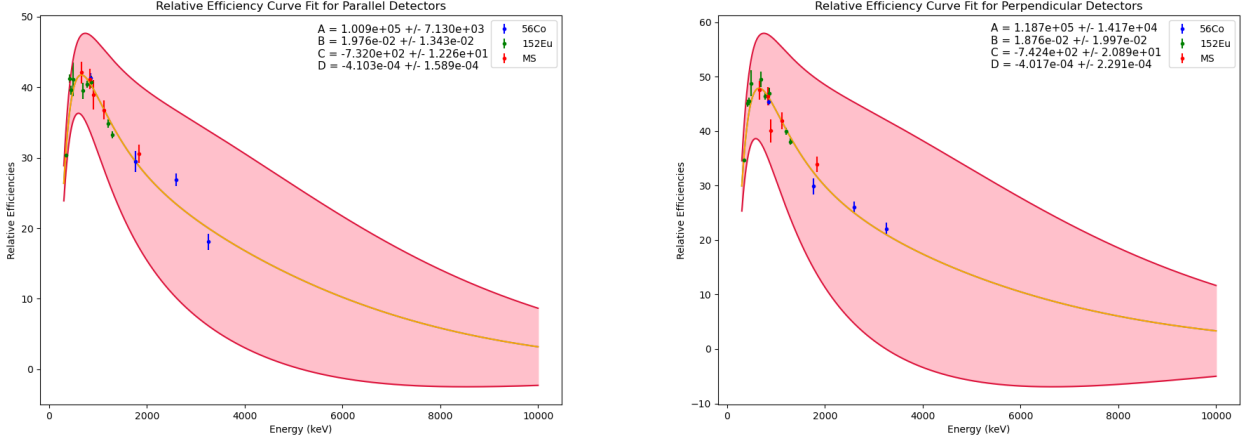
FIG. 16: Relative efficiency curve fits of Eq. 16 for the parallel detectors (left) and the perpendicular detectors (right). The relative efficiency curve is in yellow, while the area of uncertainty is marked in pink. In both detectors, the uncertainty is large due to only having few data points at higher energies, a poor model for the relative efficiency dependence on energy, and using three calibration sources rather than one.
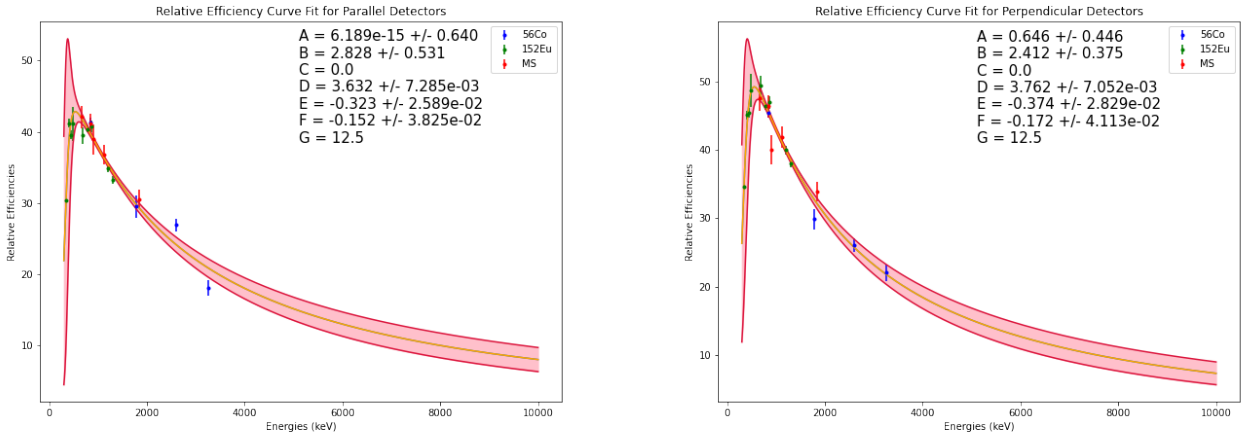

FIG. 17: Relative efficiency curve fits of Eq. 17 for the parallel detectors (left) and the perpendicular detectors (right). The relative efficiency curve is in yellow, while the area of uncertainty is marked in pink. Compared to the relative efficiency curves fit to Eq. 16, the uncertainty in these fits are much improved. The parameters to Eq. 17 is provided in the top right corners.

C. Branching Ratios

The branching ratios for the decay from the 10.71-MeV excited state in ^{24}Mg were found using data from the MgO + Nothing runs. A single partial width for a given decay from state i to state j, $\Gamma_{i \to j}$, is:

$$\Gamma_{i \to j} = \frac{N_{\parallel, i \to j}}{W_{0 \to i \to j} \epsilon_{\parallel}(E_{\gamma, i \to j})} + \frac{N_{\perp, i \to j}}{W_{0 \to i \to j} \epsilon_{\perp}(E_{\gamma, i \to j})} \tag{18}$$

in which $N_{p, i \to j}$ is the number of counts for decay $i \to j$ in detector p and $W_{0 \to i \to j}$ is the angular distribution of the excitation and decay cascade.

The angular distribution for a decay is dependent on the decay mode, which is dependent on the spins and polarities

TABLE IV: List of the energy of the emitted γ ray, the spin and parity of their initial state J_i^π and final state J_f^π, and the decay's mixing ratio δ.

E_γ(keV)	J_i^π	J_f^π	$|\delta|$	Transition
10703.71(4)	1^+	0^+	0	Pure M1
9336.15(28)	1^+	2^+	0	Pure M1
6468.6(4)	1^+	2^+	0	Pure M1
4277.4(4)	1^+	0^+	0	Pure M1
2960.1(9)	1^+	1^+	1	Equal mixture of M1 and E2

TABLE V: The table presents the energy of the initial excited state, E_i, as well its the spin and parity J_i^π. It also lists the energy of the emitted γ ray, E_γ, the energy of the final level after decay, E_f, and its spin and parity J_f^π. Finally, the branching ratios are listed in the final column.

E_i [keV]	J_i^π	E_γ [keV]	E_f [keV]	J_f^π	Branching Ratio
10712	1^+	10703.71(4)	0.0	0^+	0.733(49)
		9336.15(28)	1368.667(5)	2^+	0.205(41)
		6468.6(4)	4238.35(4)	2^+	0.0392(77)
		4277.4(4)	6432.2(10)	0^+	0.0149(32)
		2960.1(9)	7747.7(2)	1^+	0.0076(16)

of the initial, excited, and final states. For the cascades I am examining, the decay to the final state could be dipole, quadrupole, or mixed in character. The ratio between the dipole and quadrupole decays is characterized by the mixing ratio δ, but is unknown for the decays in Fig. 9. I used the spins and polarities of the decay states given in Ref [18], the resultant counts for those decays in the parallel and perpendicular detectors, and the angular distributions for decay cascades in [10] to provide an estimate of the decay mixing ratios. These can be found in Table. IV. The $E_\gamma = 10703$ keV and $E_\gamma = 4277$ keV transitions must be pure dipoles, $\delta = 0$, since these are associated with $1^+ \rightarrow 0^+$ transitions. I assumed the $E_\gamma = 9336$ keV and $E_\gamma = 6468$ keV transitions were also pure dipole ones because the excited states involved are known to correspond to neutron excitations whose decays are dominated by M1 mulitpolarities. The $E_\gamma = 2960$ keV transition was a bit trickier to determine. With the knowledge that the decay produced few emissions in the parallel detectors, from Fig. 11, I used Ref. [10] to find that this would happen for this transition when $\delta = 1$. Implementation of these angular distributions was carried out with the alpaca python package on GitHub made by Udo Friman-Gayer.

VI. RESULTS

After fitting and integrating Gaussian peaks from the parallel and perpendicular detector histograms in the MgO + Nothing runs, I calculated the branching ratios of the 10.71-MeV state with Eq. 18. These branching ratios are listed in Table V.

From the values of Table V, it makes sense why the $E_\gamma = 9336$, 6468, 4277, and 2960 keV transitions were not seen in experiments done with a bremmsstrahlung beam. If a photon excites ^{24}Mg to its 10.71-MeV excited state, it has a 20.5%, 3.92%, 2.49%, and 0.76% chance of decaying through those unseen transitions, respectively. This highlights the power of using the quasi-monochromatic photon beam, produced at HIγS, to better define the various decay modes of a given state.

The full level scheme of the transitions from the 10.71-MeV excited state are illustrated in Fig. 18. Cascades denoted by a black arrow are present in my spectra and listed in the NNDC data sheets. Cascades denoted by a dashed gray line were not present in my spectra, but were listed in the NNDC data sheets. While I did see the $E_\gamma = 6.38$ MeV transition from the 7.74-MeV excited state, I did not observe the $E_\gamma = 7.746$ MeV and 3.509 MeV
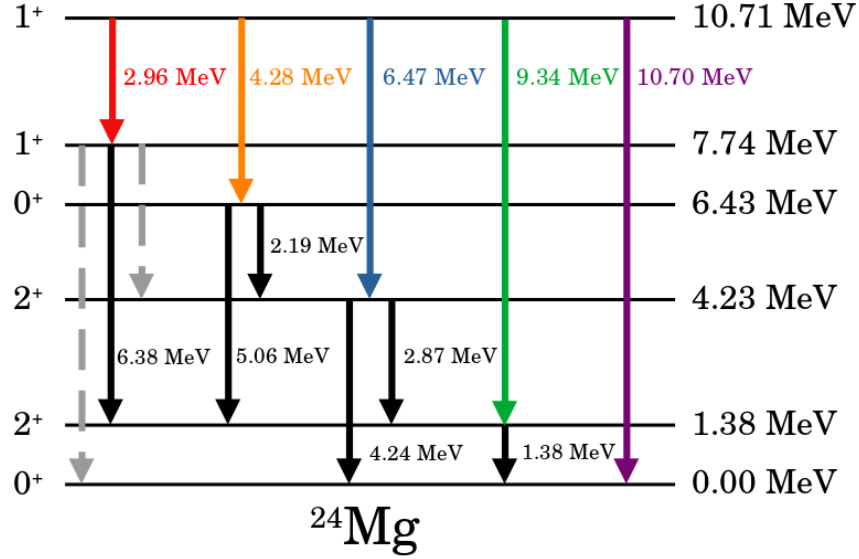
FIG. 18: The level scheme of the 10.71-MeV excited state in ^{24}Mg. The transitions from the 10.71-MeV state are colored, the cascades to the ground state that were found are black, and the ones that are listed in the NNDC that were not found are gray and striped.

ones. According to the NNDC, these states have relative intensities of 100(3)%, 39(3)%, and 12.9(9)% respectively [13]. It makes sense that I would not see the lowest intensity transitions, from the 7.74-MeV state, cascading from the least intense decay, from the 10.71-MeV level.

Using the MgO + Nothing run, I found the experimental asymmetry, for the elastic decay to ground state, to be $\bar{A}_{ex,c} = 0.941(2)$. This supports the claim that this cascade has the toroid-like angular distribution seen in Fig. 3, resulting in an experimental asymmetry $\bar{A}_{ex,c} \approx 1$. This experimental asymmetry measured when just the central target is present being close to one also supports the reliability of my formula for the experimental asymmetry, Eq. 4. More importantly, this value of $\bar{A}_{ex,c}$ confirms the spin and parity of the 10.71 MeV state to be 1^+, an important result of this work.

I found the experimental asymmetry of the MgO + MgO runs to be $\bar{A}_{Ex} = 0.644(5)$ while the mass-weighted asymmetry to be $\bar{A}_{MW} = 0.457(5)$. Thus, this analysis clearly shows that self-absorption is taking place.

As of right now, I cannot confidently finalize a result for the full and partial widths of the 10.71 MeV state due to my results of Eq. 8 not aligning with predicted values. Currently, I find that $\bar{A}_{eff} = 0.330(21)$, which is lower than expected and does not equal A_{Ex}, no matter how large my total resonance width is. This alarms me because increasing the total resonance width of the 10.71 MeV state results in the central target experiencing more resonant scattering, reducing the scattering off the downstream one and increasing $\bar{A}_{eff}$. However, when increasing the total resonance width, $\bar{A}_{eff}$ levels off too quickly, indicating that this effect is not being seen.

There are two possible issues which could account for the discrepancy. These are currently being investigated. The first is that the calculation of $\langle \Phi^\tau \sigma \rho_A^\tau \rangle$ is not properly accounting for the reduced photon flux of the beam before reaching at the downstream target. This would explain why increasing the total resonance width does not have the expected effect on $\bar{A}_{eff}$. The second is that there was an inconsistency in the simulations. My experimental asymmetry when just the downstream target was present is $\bar{A}_{Ex,d} = 0.246(7)$, which differs greatly from my effective asymmetry for the downstream target alone by a factor of about 2.2. However, the same behavior is not observed in the experimental and effective asymmetries when only the central target is present, indicating an error lies in the calculation of the downstream target's asymmetry. When scaling the effective asymmetry when both targets are present upwards by 2.2, the full width is found to be about 2 eV. This discrepancy could come from improper simulations. Unfortunately, no definitive reason has yet been found as to why $\bar{A}_{eff}$ is not following expected trends.

VII.   DISCUSSION AND CONCLUSIONS

In determining the asymmetry coefficients, I obtained important results regarding the decay properties of the 10.71-MeV state such as confirming its spin and parity, as well as observing five decay branches and their branching ratios. This was made possible with the linearly polarized quasi-monochromatic photon beam produced at HIγS. The reduced background, as compared to a bremmsstrahlung beam, allowed me to confidently observe the low-intensity transitions to the $E_f = 1368$, 4238, 6432, and 7747 keV states. The linear polarization resulted in angular distributions that I could compare to Ref [10] and herewith confirm spins and parities of the involved states. This alone shows the immense power and potential HIγS has in probing states in other isotopes.

As seen in Section VI, values of $\bar{A}_{Ex} = 0.644(5)$ and $\bar{A}_{MW} = 0.457(5)$ were found. The difference between the two asymmetries indicates that self absorption is taking place in the MgO + MgO runs. The $\bar{A}_{MW}$ coefficient is essentially a weighted average between the $\bar{A}_{Ex,c}$ and $\bar{A}_{Ex,d}$ ones. As stated earlier, due to the position of the the downstream target compared to the central one, the coefficient $\bar{A}_{Ex,d}$ is going to be less than the $\bar{A}_{Ex,c}$ one. However, since the central target is not present in the run used in calculating the $\bar{A}_{Ex,d}$ value, there is no absorption of the photon beam, resulting in more excitations, emissions, and detected γ rays from the downstream target as compared to when both are present. Therefore, the lesser $\bar{A}_{Ex,d}$ coefficient is weighted more in the calculation of the $\bar{A}_{MW}$ value. If absorption was not taking place between the targets, the $\bar{A}_{Ex}$ coefficient would be approximately equal to the $\bar{A}_{MW}$ one. This proves that self absorption is taking place between the central and downstream targets, and validates the use of this technique. While it may seem obvious that this would be true, there was no guarantee that the central target would absorb a number of resonant photons sufficient to make a noticeable difference in the emissions from the downstream target. Nor could one assume that the increased mass of the downstream target would not completely offset the lower count rate caused by the reduced photon flux. Since there is a noticeable difference between the $\bar{A}_{Ex}$ and $\bar{A}_{MW}$ values, these assumptions can now be made with confidence. Therefore, there is sufficient grounds for the PSA method to work.

As stated above, current calculations for the $\bar{A}_{eff}$ coefficient indicate that the value asymptotically levels off as the total resonance width of the 10.71-MeV state is increased indefinitely. At first, this seemed contrary to theory, as increasing the total resonance width Γ_i should result in more photons resonantly scattering off the central target; therefore, the downstream one should experience fewer excitations. This, however, is not fully correct.

Due to the thermal motion of the nucleus within the crystal lattice, there will be a Doppler shift in the energy of the emitted photons. This results in a widening of the resonance width, denoted by the Doppler width, Δ, in Ref. [3]:

$$\Delta = \sqrt{\frac{2k_B T_{eff}}{Mc^2}} E_r \tag{19}$$

in which k_B is the Boltzmann constant, T_{eff} is the effective temperature of the sample, M is the mass of the sample, c is the speed of light, and E_r is the resonance energy. In the short lifetime limit, when condensed matter effects are not present, $\Gamma_i >> \Delta$, the on-resonance absorption cross section, as defined by Ref. [3], is:

$$\sigma_0 \propto \frac{\Gamma_0}{\Gamma_i} \tag{20}$$

In the calculation of the $\bar{A}_{eff}$ asymmetry, Γ is being increased such that the $\bar{A}_{eff}$ and $\bar{A}_{Ex}$ coefficients equate. However, from Eq. 20, it can be seen that simultaneously increasing Γ_0 and Γ_i has no effect on the on-resonance absorption cross section. This can best be explained with Fig. 1. Increasing the total resonance width results in more photons that can resonantly excite a nucleus; so, the dips in the photon flux at resonant energies in Fig. 1 would get wider, but not deeper. Therefore, the downstream target would experience the same number of resonant excitations with respect to the central target. Since the effective asymmetry is a ratio of two energy integrals, this would explain

why the $\bar{A}_{eff}$ coefficient levels off rather than approach 1 as the total resonance width is increased indefinitely.

In the long lifetime limit when condensed matter effects are present, $\Gamma_i << \Delta$, the effective absorption cross section, as defined by Ref. [3], is:

$$\sigma_a \propto \Gamma_0 \tag{21}$$

indicating that the increasing Γ_i, and thus Γ_0, would deepen the resonance, resulting in more photons being absorbed by the central target. This would explain why the effective asymmetry does not exhibit the asymptotic leveling when decreasing the total resonance width. Therefore, equations 20 and 21 show that the asymptotic leveling of the effective asymmetry is predicted by theory.

The branching ratios given in Table V are a good indication of why over half the decay modes from the 10.71-MeV level were not previously known. The $E_\gamma = 4277.4$ keV and $E_\gamma = 2960.1$ keV decays were, respectively, 50 and 96 times less likely to occur, compared to the previously known ground state decay. It would make sense that these low-intensity decay modes were not seen in experiments done with a bremsstrahlung beam. There were some instances in which these peaks were difficult for me to find, even with the reduced background from the quasi-monochromatic photon beam. They were most likely drowned out by the large nonresonant background radiation demonstrated in Fig. 2, explaining why these decay modes were not found in prior investigations.

After completing the data analysis, there are a few changes that I would make if PSA was to be used again. First, fitting the peaks for the three calibration sources and scaling the relative efficiencies to each other took a significant amount of time that could have been avoided if a stronger source was used. Samantha Johnson, a colleague of mine, used the same ^{56}Co source as her calibration standard, but her experiment was about a year prior to mine. Unlike my spectra, in which I could only use three peaks from the ^{56}Co spectra, Samantha was able to maximize ^{56}Co and use fifteen peaks. Not only would using one calibration source save time, it would also eliminate the error associated with scaling the other calibration sources' relative efficiency curves.

Another modification I would make would be to actively watch and keep track of the gain of the detectors during the experiment to ensure that disfigurement of decay peaks, as seen in Fig. 10, would not permeate a portion of the experiment. Consequently, I would not have had to use the less desirable integrate function to find the volume of peaks within the parallel detectors for the runs involving MgO.

Finally, to find the branching ratios for an excited state, I would have done a MgO + Nothing run with circular beam polarization to avoid having to estimate mixing ratios. The original author of the PSA method had intended to use current models and knowledge to get the branching ratios rather than calculate them in the experiment. However, in situations where current knowledge lacks for all decays from a state, such as the case for the 10.71-MeV excited state in ^{24}Mg, this approach fails. The MgO + Nothing run done in the experiment used a linearly polarized beam, which, of course, results in a well defined angular correlation associated with the emission. When calculating the branching ratios, I needed to know the mixing ratios of the examined transitions, but if the decay has not yet been determined, I needed to evaluate a mixing ratio based on the number of counts found in the detectors. By completing a run with a circularly polarized beam, those angular correlations, and therefore the mixing ratios, would not have been required.

VIII.   ACKNOWLEDGEMENTS

resources to complete a senior honors thesis.

---

[1] J. Isaak, D. Savran, B. Löher, T. Beck, M. Bhike, U. Gayer, Krishichayan, N. Pietralla, M. Scheck, W. Tornow, V. Werner, A. Zilges, and M. Zweidinger, Physics Letters B **788**, 225 (2019).

[2] A. Banu, E. G. Meekins, J. A. Silano, H. J. Karwowski, and S. Goriely, Physical Review C **99** (2019), 10.1103/physrevc.99.025802.

[3] A. Zilges, D. Balabanski, J. Isaak, and N. Pietralla, Progress in Particle and Nuclear Physics **122**, 103903 (2022).

[4] S. Goriely, P. Dimitriou, M. Wiedeking, T. Belgya, R. Firestone, J. Kopecky, M. Krtička, V. Plujko, R. Schwengner, S. Siem, H. Utsunomiya, S. Hilaire, S. Péru, Y. S. Cho, D. M. Filipescu, N. Iwamoto, T. Kawano, V. Varlamov, and R. Xu, The European Physical Journal A **55**, 172 (2019).

[5] U. Kneissl, H. Pitz, and A. Zilges, Progress in Particle and Nuclear Physics **37**, 349 (1996).

[6] U. Friman-Gayer, A. D. Ayangeakaa, D. Gribble, C. Iliadis, X. James, R. F. F. Janssens, S. Johnson, A. Saracino, and N. Sensharma, "Efficient self-absorption experiments using polarized photon beams," (2021).

[7] F. R. Metzger, Phys. Rev. **103**, 983 (1956).

[8] C. Romig, *Investigation of Nuclear Structure with Relative Self-Absorption Measurements*, Ph.D. thesis, Darmstadt, Tech. Hochsch. (2015).

[9] D. Savran and J. Isaak, Nuclear Instruments and Methods in Physics Research Section A: Accelerators, Spectrometers, Detectors and Associated Equipment **899**, 28 (2018).

[10] C. Iliadis and U. Friman-Gayer, The European Physical Journal A **57** (2021), 10.1140/epja/s10050-021-00472-1.

[11] N. Pietralla, Z. Berant, V. N. Litvinenko, S. Hartman, F. F. Mikhailov, I. V. Pinayev, G. Swift, M. W. Ahmed, J. H. Kelley, S. O. Nelson, R. Prior, K. Sabourov, A. P. Tonchev, and H. R. Weller, Phys. Rev. Lett. **88**, 012502 (2001).

[12] U. Friman-Gayer, "Self-absorption experiments with polarized photon beams, private communication," (2021).

[13] R. Firestone, Nuclear Data Sheets **108**, 2319 (2007).

[14] D. Gribble, C. Iliadis, R. V. F. Janssens, U. Friman-Gayer, N. Krishichayan, and S. Finch, Physical Review C **106** (2022), 10.1103/physrevc.106.014308.

[15] G. Rusev, A. P. Tonchev, R. Schwengner, C. Sun, W. Tornow, and Y. K. Wu, Phys. Rev. C **79**, 047601 (2009).

[16] J. Kelley, E. Kwan, J. Purcell, C. Sheu, and H. Weller, Nuclear Physics A **880**, 88 (2012).

[17] M. Wang, W. Huang, F. Kondev, G. Audi, and S. Naimi, Chinese Physics C **45**, 030003 (2021).

[18] J. Deary, M. Sheck, R. Schwengner, D. O'Donnell, R. Bemmerer, R. Beyer, T. Hensel, A. Junghans, T. Kogler, S. E. Muller, K. Romer, K. Schmidt, S. Turkat, S. Urlab, A. Wagner, M. Bowry, P. Adsley, O. Ogar, R. Chapman, F. C. L. Crespi, D. T. Doherty, U. F. Gayer, R.-D. Herzberg, J. Issak, R. V. F. Janssens, T. Kroll, B. Loher, S. N. S. Bondili, P. von Neumann-Cosel, L. Pellegri, E. E. Peters, G. Rainovski, D. Savran, J. F. Smith, M. Spieker, P. G. Thirolf, S. Triambak, W. Tornow, M. Venhart, M. Wiedeking, O. Wieland, S. W. Yates, and A. Zilges, "Photo-response of the $n = z$ nucleus ^{24}mg," private communication and to be published (2022).

[19] G. Peckham, Proc. Phys. Soc. (London), 90: 657-70(Mar. 1967). (1967), 10.1088/0370-1328/90/3/312.

[20] W. E. Lamb, Phys. Rev. **55**, 190 (1939).

[21] K. S. Singwi and A. Sjölander, Phys. Rev. **120**, 1093 (1960).

[22] U. Friman-Gayer, C. Romig, T. Hüther, K. Albe, S. Bacca, T. Beck, M. Berger, J. Birkhan, K. Hebeler, O. J. Hernandez, J. Isaak, S. König, N. Pietralla, P. C. Ries, J. Rohrer, R. Roth, D. Savran, M. Scheck, A. Schwenk, R. Seutin, and V. Werner, Phys. Rev. Lett. **126**, 102501 (2021).

[23] U. Friman-Gayer and op3, "Ries: Resonances integrated over energy and space,".

[24] A. Shelby, U. Friman-gayer, and R. V. F. Janssens, "New method of self-absorption: Demonstrating utility of a polarized photon beam, private communication,".

[25] U. Friman-Gayer, en*Probing Nuclear Structure Relevant for Neutrinoless Double-Beta Decay with Nuclear Resonance Fluorescence*, Ph.D. thesis, Technische Universität, Darmstadt (2020).

[26] D. C. Radford, "Notes on the use of the program gf3," (2001).